



**HAL**  
open science

## Silver Doping Mechanism in Bioceramics-From Ag<sup>+</sup>: Doped HAp to Ag<sup>0</sup>/BCP Nanocomposite

Aurélie Jacobs, Morgane Gaulier, Alexis Duval, Guillaume Renaudin

► **To cite this version:**

Aurélie Jacobs, Morgane Gaulier, Alexis Duval, Guillaume Renaudin. Silver Doping Mechanism in Bioceramics-From Ag<sup>+</sup>: Doped HAp to Ag<sup>0</sup>/BCP Nanocomposite. *Crystals*, 2019, 9 (7), pp.326. 10.3390/cryst9070326 . hal-02194805

**HAL Id: hal-02194805**

**<https://hal.science/hal-02194805v1>**

Submitted on 18 Dec 2020

**HAL** is a multi-disciplinary open access archive for the deposit and dissemination of scientific research documents, whether they are published or not. The documents may come from teaching and research institutions in France or abroad, or from public or private research centers.

L'archive ouverte pluridisciplinaire **HAL**, est destinée au dépôt et à la diffusion de documents scientifiques de niveau recherche, publiés ou non, émanant des établissements d'enseignement et de recherche français ou étrangers, des laboratoires publics ou privés.

1 Article

# 2 Silver doping mechanism in bioceramics – from 3 Ag<sup>+</sup>:doped HAp to Ag<sup>0</sup>/BCP nanocomposite

4 Aurélie Jacobs<sup>1</sup>, Morgane Gaulier<sup>1</sup>, Alexis Duval<sup>1</sup> and Guillaume Renaudin<sup>1\*</sup>

5 <sup>1</sup> Université Clermont Auvergne, CNRS, SIGMA Clermont, ICCF, F-63000 Clermont-Ferrand, France.

6 \* Correspondence: guillaume.renaudin@sigma-clermont.fr; Tel.: 00 33 4 73 40 73 36, Fax.: 00 33 4 73 40 70 95

7 Received: date; Accepted: date; Published: date

8 **Abstract:** The results presented in this paper, based on the powder X-ray diffraction technique  
9 followed by Rietveld analyses, are devoted to the mechanism of silver incorporation in Biphasic  
10 Calcium Phosphates. Results were confirmed by SEM observation. Samples were synthesized via  
11 the sol-gel route, followed by heat treatments. Two incorporation sites were highlighted: Ca<sup>2+</sup>  
12 replacement by Ag<sup>+</sup> into the calcium phosphates (HAp: hydroxyapatite and β-TCP: TriCalcium  
13 Phosphate), and the other as metallic silver Ag<sup>0</sup> nanoparticles (formed by autogenous reduction).  
14 The samples obtained were thus nanocomposites, written Ag<sup>0</sup>/BCP, composed of closely-mixed Ag<sup>0</sup>  
15 particles of about 100 nm at 400 °C (which became micrometric upon heating) and calcium  
16 phosphates, themselves substituted by Ag<sup>+</sup> cations. Between 400 °C and 700 °C the cationic silver  
17 part was mainly located in the HAp phase of the composition Ca<sub>10-x</sub>Ag<sub>x</sub>(PO<sub>4</sub>)<sub>6</sub>(OH)<sub>2-x</sub> (written  
18 Ag<sup>+</sup>:HAp). From 600 °C silver cations migrated to β-TCP to form the definite compound  
19 Ca<sub>10</sub>Ag(PO<sub>4</sub>)<sub>7</sub> (written Ag<sup>+</sup>:TCP). Due to the melting point of Ag<sup>0</sup>, the doping element completely  
20 left our sample at temperatures above 1000 °C. In order to correctly understand the biological  
21 behaviour of such material, which is potentially interesting for biomaterial applications, its complex  
22 doping mechanism should be taken into consideration for subsequent cytotoxic and bacteriologic  
23 studies.

24 **Keywords:** Biomaterial; Silver-doping; Silver nano-composite; Hydroxyapatite; Powder X-ray  
25 Diffraction.

26

## 27 1-. Introduction

28 The utilization of synthetic materials for bone reconstructive surgery is generally necessary,  
29 because autograft and allograft practice is limited by the quantity of available material, and in the  
30 first case entails a second surgical procedure [1]. Among the numerous synthetic materials  
31 investigated for bone replacement and/or prosthesis coating, hydroxyapatite (HAp, Ca<sub>10</sub>(PO<sub>4</sub>)<sub>6</sub>(OH)<sub>2</sub>)  
32 is the most often-used material due to its chemical and structural similarities with the bone mineral  
33 constituent [2-5]. Biological apatite refers to the main constituent of bone and hard tissue in mammals:  
34 a poorly crystallized non-stoichiometric carbonate-containing HAp that composes about 65 weight  
35 percent (wt %) of bone and about 90 wt % of dental enamel [6]. Apatite is a complex and diverse class  
36 of materials, with a flexible structure that accepts many substitutions, either cationic or anionic [7].  
37 Hydroxyapatite is therefore an interesting biocompatible and osteoconductive material, but it has  
38 limited antibacterial properties [8], even though bacterial infections are the main cause of  
39 postoperative problems [9]. Bacterial overgrowth on the surface of orthopaedic implants – that is,  
40 biofilm formation – potentially leads to serious complications during reconstructive surgery, with  
41 severe physiological damage, significant patient discomfort and additional costly surgical  
42 procedures [10-12]. About 1% of total joint hip arthroplasties, and about 3% in the case of knees,

43 require a second (or multiple) surgical intervention(s) because of bone healing process complications,  
44 which makes it a real societal problem on a global scale [13-17]. Nowadays, an antibacterial effect at  
45 the surgical site is ensured by systematic antibiotic administration via the blood, which potentially  
46 generates toxicity, poor penetration into the surgical site, and also the problem of bacterial resistance.  
47 The delivery, or the presence, of a bactericidal agent directly at the surgical site would ensure a really  
48 promising alternative [18,19]. Among the various possibilities, the use of silver – well known in  
49 medicine since ancient times in the treatment of bacterial infection – seems very promising by  
50 combining broad spectrum and long term antimicrobial activity with the absence of microorganisms  
51 developing resistance [20-25]. A particularity of the antiseptic properties of silver is the possibility of  
52 using it in metallic or ionic form, without a loss of efficiency [26-28,41]. For these reasons, research  
53 on silver incorporation into hydroxyapatite has developed in recent years, and has shown the high  
54 potential of the synthesized materials [17,22,29-35]. Although the results agree regarding the  
55 beneficial biological effects, the literature on the topic does not address the fine description of the  
56 synthesized materials and the mechanisms of silver incorporation. Many synthesis methods have  
57 been described (co-precipitation [29,35,43] potentially followed by a thermal [8,22,33,36,38] or  
58 reducing treatment [34,41], sol-gel [17,30,40,44], electrochemical [31,37]; hydrothermal [32],  
59 microwave [26,39], sonochemical [42], plasma-spraying [43,45] and also impregnation [46,47]  
60 methods), with the formation of two different kinds of material: either an Ag<sup>+</sup>:doped HAp compound  
61 or an Ag<sup>0</sup>/HAp nanocomposite material. The difference is – of course – fundamental, since in the first  
62 case the single-phase material contains Ag<sup>+</sup> cations that substitute Ca<sup>2+</sup> from the HAp crystal  
63 structure, while in the second case metallic silver particles are intimately mixed in a multi-phase  
64 composite. Although these two alternatives are listed and described in the literature [42] there is a  
65 lack of understanding the mechanisms that lead to one or the other.

66 The purpose of this paper is to fully characterize the silver-HAp doping mechanism in the case  
67 of sol-gel synthesis followed by gradual thermal treatment leading to silver auto-reduction. The  
68 study is a continuation of our previous work on the BCP (biphasic calcium phosphate) doping  
69 mechanism with cations from the first-row transition metals [48]. The case of zinc doping, with an  
70 interstitial mode of incorporation into the HAp crystal structure, was first fully characterized [49-51],  
71 then investigated for iron [52]. In the case of copper, it transpired that control of the doping  
72 mechanism allowed an insight into behaviour in a biological environment [53]. For a complete  
73 understanding of the present paper it is very important to note the difference between the notations  
74 used: Ag<sup>+</sup>:HAp and Ag<sup>0</sup>/HAp. Ag<sup>+</sup>:HAp corresponds to the incorporation of Ag<sup>+</sup> cations within the  
75 crystal structure of hydroxyapatite (which is expected in the case of conventional cationic doping),  
76 whereas Ag<sup>0</sup>/HAp means the formation of a composite containing two distinct phases, the  
77 hydroxyapatite trapping nanoparticles of Ag<sup>0</sup> metallic silver.

## 78 2-. Materials and methods

### 79 2.1. Sol-gel elaboration of silver containing BCP samples

80 The sol-gel route previously proposed by the authors was used to synthesize both undoped and  
81 Ag-doped series of BCP samples [51]. Briefly, to produce 2 g of undoped BCP powder, 4.7 g of  
82 Ca(NO<sub>3</sub>)<sub>2</sub>·4H<sub>2</sub>O (Sigma-Aldrich) and 0.84 g of P<sub>2</sub>O<sub>5</sub> (Sigma-Aldrich) were dissolved in ethanol under  
83 stirring and refluxed at 85°C for 24 hours. The solution was then maintained at 55°C for 24 hours to  
84 obtain a white consistent gel, and further heated at 80°C for 10 hours to obtain a white powder.  
85 Finally, the powder was heat-treated for 15 hours. This thermal treatment was performed between  
86 100°C and 1200°C. Samples from the undoped series were named the 0Ag-*T* series with *T* indicating  
87 the temperature (from 400°C to 1200°C) of the following thermal treatment. Required amounts of  
88 AgNO<sub>3</sub> (Sigma-Aldrich) were added to the solution simultaneously with Ca(NO<sub>3</sub>)<sub>2</sub>·4H<sub>2</sub>O (Sigma-  
89 Aldrich) in order to synthesize the Ag-doped series. Nominal compositions were calculated,  
90 assuming Ag<sup>+</sup> calcium substitution (i.e. assuming a (Ca+Ag)/P = 1.67 constant ratio) with two doping  
91 levels: a 2.5% calcium substitution (Ag/(Ca+Ag) = 0.025 corresponding to the nominal composition  
92 Ca<sub>9.75</sub>Ag<sub>0.25</sub>(PO<sub>4</sub>)<sub>6</sub>(OH)<sub>1.75</sub>; named the 25Ag-*T* series) and a 10% calcium substitution (Ag/(Ca+Ag) = 0.1

93 corresponding to the nominal composition  $\text{Ca}_9\text{Ag}_1(\text{PO}_4)_6(\text{OH})$ ; named the 100Ag-*T* series). As-  
94 synthesized Ag-doped powders were pale yellow; heat treatments turn the colour to light grey, and  
95 then to white above 1000°C.

## 96 2.2. Powder X-Ray Diffraction (PXRD) and Rietveld analyses

97 PXRD patterns were recorded on a Philips X'Pert Pro PANalytical diffractometer (Almelo,  
98 Netherlands), with  $\theta$ - $\theta$  geometry, reflection mode, equipped with a solid-state X-Celerator detector  
99 and using Cu K $\alpha$  radiation ( $\lambda = 1.54184 \text{ \AA}$ ). PXRD patterns were recorded at room temperature in the  
100 interval  $3^\circ < 2\theta < 120^\circ$ , with a step size of  $\Delta 2\theta = 0.0167^\circ$  and a counting time of 200s for each data  
101 value.

102 Rietveld refinements were systematically performed for each measurement (13 temperatures for  
103 the 3 series) using the FullProf.2k program [54]. The Rietveld strategy was detailed in previous  
104 related works [48-53]. A new additional phosphate compound was considered here:  $\text{AgCa}_{10}(\text{PO}_4)_7$ ,  
105 which crystallizes in the trigonal  $R3c$  space group with  $a = 10.4372 \text{ \AA}$  and  $c = 37.3379 \text{ \AA}$  [55]. It is  
106 isotopic with members of the  $M\text{Ca}_{10}(\text{PO}_4)_7$  ( $M = \text{Li}, \text{Na}, \text{K}$  and  $\text{Cs}$ ) series, and is closely related to the  
107 structure of  $\beta$ -TCP ( $\beta$ - $\text{Ca}_3(\text{PO}_4)_2$ ,  $R3c$  symmetry with  $a = 10.4352 \text{ \AA}$  and  $c = 37.4029 \text{ \AA}$  [56]). The half-  
108 occupied Ca4 site of  $\beta$ -TCP [56], becomes fully occupied by silver cations in  $\text{AgCa}_{10}(\text{PO}_4)_7$  [55];  
109 explaining the charge compensation between  $\text{Ca}^{2+}$  and  $\text{Ag}^+$ . The metal  $\text{Ag}^\circ$  phase was also considered  
110 in several sample; it is a compact cubic structure  $Fm\bar{3}m$  with  $a = 4.085 \text{ \AA}$  [57]. An example of a  
111 Rietveld plot is shown in Figure SEI1.

## 112 2.3. Scanning Electron Microscopy (SEM)

113 Electronic microscopy observations used a ZEISS SUPRA 55VP with GEMINI Field Emission –  
114 Scanning Electron Microscope and were carried out on pressed pellets after gold metallization. No  
115 polishing was carried out to avoid the leaching of the silver cations and to avoid the deformation of  
116 the ductile metallic silver particles. The main object of this analysis is not the quantification, but the  
117 localization, of the silver element. Quantitative analyses were performed using an EDS (OXFORD  
118 XMAX 80 N+ 80 mm<sup>2</sup> Si-detector combined with OXFORD AZtec Advanced V3.3 software) on Ca, P  
119 and Ag elements. Measurements were made using an acceleration voltage of 20 kV and 30 seconds  
120 of acquisition on three wide areas (magnification x100) before averaging. Some specific isolated  
121 measurements were performed using x5000 magnification. A 4QBSD detector was used to acquire  
122 chemical contrast images to highlight silver particles.

123 The following nine samples were characterized by SEM: 0Ag-400, 0Ag-700, 0Ag-1200, 25Ag-400,  
124 25Ag-700, 25Ag-1200, 100Ag-400, 100Ag-700 and 100Ag-1200.

## 125 3-. Results: Materials characterization

### 126 3.1. Quantitative phase analysis

127 To correctly interpret the behaviour of our samples, their phase compositions were extracted  
128 from Rietveld analyses (PXRD patterns from the 25Ag-*T* series are shown in Figure 1). Figure 1  
129 evidences the gradual increase in crystallinity of HAP with respect to temperature by the decrease in  
130 the diffraction peak width. Phase compositions of the undoped BCP series and of the two Ag-doped  
131 BCP series ( $x = 25$  and  $100$ ) are presented in Table 1, and Figure 2a represents the thermal composition  
132 variation for the two main phases: HAP and  $\beta$ -TCP. Supplementary minor phases were observed.  $\alpha$ -  
133 CDP (diCalcium DiPhosphate with composition  $\text{Ca}_2\text{P}_2\text{O}_7$ ) was observed up to 700°C, with a  
134 maximum amount of 4 wt % at 500-600°C. CaO and  $\text{CaCO}_3$  (calcite) were present in the samples.  
135 They are indicated in CaO equivalent content in Table 1, as calcite decarbonation leads to CaO  
136 formation at about 800°C. The amount of CaO equivalent becomes negligible at high temperatures,  
137 where the BCP were mainly composed of HAP (corresponding to the nominal composition). All these  
138 observations – on main and minor phases – were similar to those of our previous studies on first-row  
139 transition metal doping [48-53]. The  $\beta$ -TCP phase is stabilized for intermediate temperatures, with a

140 maximum amount close to 20 wt % around 900 °C for the undoped series and around 700 °C for the  
 141 two silver-doped series. The main difference compared to our previous works concerns the formation  
 142 of metallic silver, Ag<sup>0</sup>, already at 400°C in the Ag-doped series (contrary to metal oxide formation for  
 143 the first-row transition metals, including ZnO and CuO). The amount of metallic silver reached 1 wt  
 144 % for the 25Ag-*T* series and 6 wt % for the 100Ag-*T* series (Table 1 and Figure 2b). These values are  
 145 to be compared to the quantities introduced during the syntheses: 2.65 wt % for the nominal  
 146 Ca<sub>9.75</sub>Ag<sub>0.25</sub>(PO<sub>4</sub>)<sub>6</sub>(OH)<sub>1.75</sub> composition and 10.22 wt % for the nominal Ca<sub>9</sub>Ag<sub>1</sub>(PO<sub>4</sub>)<sub>6</sub>(OH) composition  
 147 (respectively the 25Ag-*T* and the 100Ag-*T* series). Figure 2b highlights the fact that the entirety of the  
 148 dopant introduced was not found exclusively in metallic form, but rather of the order of half of this  
 149 quantity. The reduction of the incorporated Ag<sup>+</sup> silver cation to Ag<sup>0</sup> silver metal was autogenous, and  
 150 monitored by the thermal treatment only, without any reducing agent.

151 The formation of Ag<sup>0</sup>/HAp nanocomposite by heating Ag<sup>+</sup>-incorporated hydroxyapatite has  
 152 already been mentioned in the literature, either using a reducing agent (NaBH<sub>4</sub> [34,58], hydrazine  
 153 [41]) or not [17,22,26,38,42]. However, the nanocomposite formation mechanism, the main subject of  
 154 this paper, has never been studied and detailed. It may first be pointed out that a thermal study on  
 155 silver nitrate (AgNO<sub>3</sub>; not shown here) showed decomposition accompanied by reduction at 300 °C,  
 156 which leads to the production of metallic silver (Ag<sup>0</sup>). To complete this information, the colour  
 157 changes of our samples are also interesting. The undoped series remained constantly white, while  
 158 the doped series were yellow at 400 °C (pale yellow for the 25Ag-*T* series and yellow-brown for the  
 159 100Ag-*T* series), then turned grey up to 1000 °C before bleaching above 1100 °C. The grey colour can  
 160 be attributed to the silver nanoparticles present in the Ag<sup>0</sup>/HAp composite. It is therefore normal to  
 161 lose the grey colour above 1000 °C, since silver has a melting point of 962 °C. Thus it is difficult to  
 162 design Ag<sup>0</sup>/HAp composites which could be obtained following heat treatments at more than 1000  
 163 °C [8,36,39,59]. Our white 25Ag-1100, 25Ag-1200 and 100Ag-1200 samples were then exempt of silver  
 164 particles, and certainly just composed of undoped HAp counterbalanced by a few wt % of β-TCP due  
 165 to the introduced Ca/P ratio (1.625 for the 25Ag-*T* series and 1.5 for the 100Ag-*T* series instead of the  
 166 1.67 value for HAp). By wetting calcium phosphate particles, metallic silver was still present in the  
 167 25Ag-1000 sample (in very little amount) and in 100Ag-1100 sample (although the Ag<sup>0</sup> amount  
 168 decrease is very clear at above 900 °C).

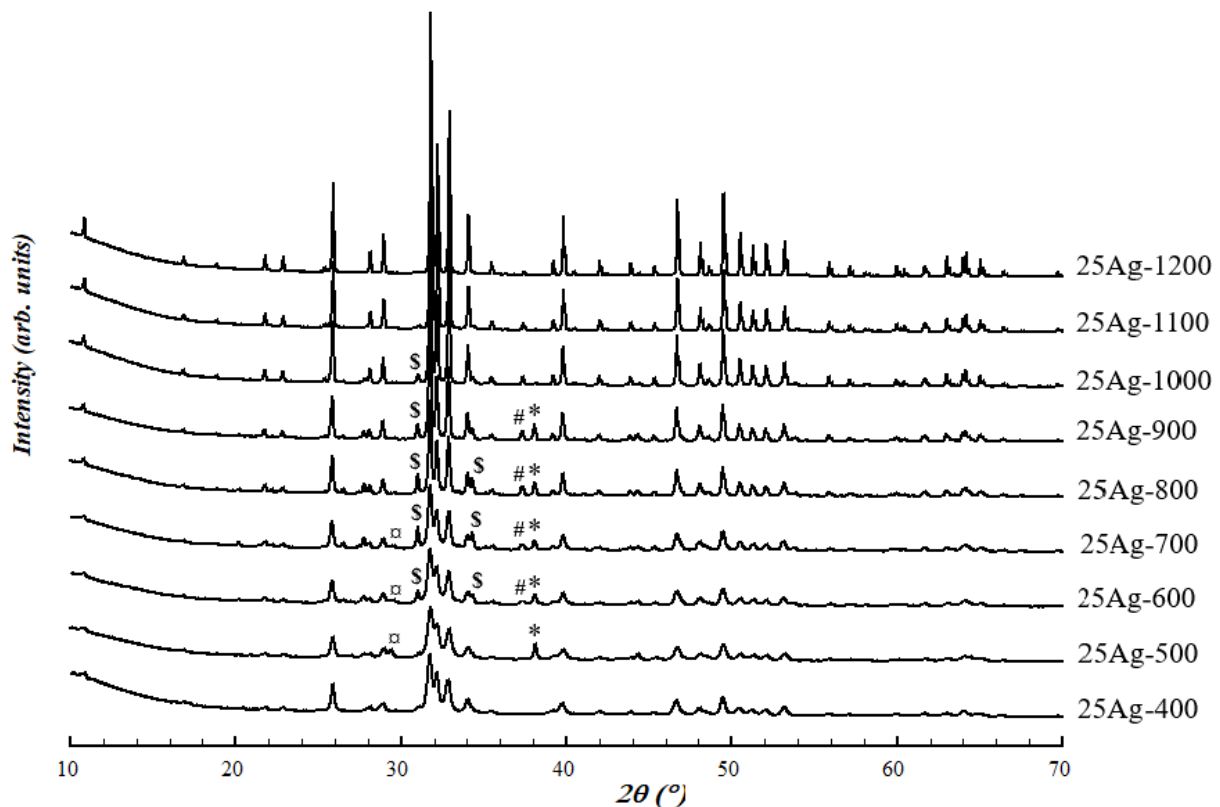
169 **Table 1.** Quantitative phase analysis (wt %) of the 27 samples; standard deviations are indicated in  
 170 brackets (CDP: Ca<sub>2</sub>P<sub>2</sub>O<sub>7</sub> and 'Eq. CaO' considers both the CaO and CaCO<sub>3</sub> amounts).

Sample	Phase composition (wt %)				
	HAp	TCP	CDP	Eq. CaO	Ag <sup>0</sup>
0Ag-400	97.1 (2.0)	2.9 (1.0)	/	/	/
0Ag-500	94.8 (2.0)	1.5 (0.5)	2.1 (0.5)	1.6 (0.5)	/
0Ag-600	91.8 (2.0)	3.3 (1.0)	3.8 (1.0)	1.2 (0.5)	/
0Ag-700	85.8 (2.0)	9.3 (1.0)	3.1 (1.0)	1.9 (0.5)	/
0Ag-800	81.9 (2.0)	16.0 (1.0)	/	2.1 (0.5)	/
0Ag-900	81.4 (2.0)	16.7 (1.0)	/	1.9 (0.5)	/
0Ag-1000	85.8 (2.0)	13.6 (1.0)	/	0.6 (0.5)	/
0Ag-1100	92.5 (2.0)	7.1 (1.0)	/	0.4 (0.2)	/
0Ag-1200	96.0 (2.0)	3.8 (1.0)	/	0.2 (0.2)	/
25Ag-400	92.7 (2.0)	2.5 (0.5)	3.1 (1.0)	1.2 (0.5)	0.3 (0.2)
25Ag-500	88.5 (2.0)	3.6 (1.0)	4.1 (1.0)	2.6 (0.5)	1.1 (0.5)
25Ag-600	81.9 (2.0)	11.3 (1.0)	3.5 (1.0)	2.4 (0.5)	0.8 (0.5)

25Ag-700	80.4 (2.0)	15.8 (1.0)	1.1 (0.5)	2.2 (0.5)	0.7 (0.5)
25Ag-800	82.9 (2.0)	14.0 (1.0)	/	2.2 (0.5)	0.9 (0.5)
25Ag-900	87.1 (2.0)	19.9 (1.0)	/	2.0 (0.5)	1.0 (0.5)
25Ag-1000	93.1 (2.0)	5.3 (1.0)	/	1.5 (0.5)	0.1 (0.2)
25Ag-1100	96.8 (2.0)	2.0 (0.5)	/	1.2 (0.5)	/
25Ag-1200	99.0 (2.0)	0.5 (0.2)	/	0.5 (0.2)	/
100Ag-400	92.3 (2.0)	/	/	2.4 (0.5)	5.3 (1.0)
100Ag-500	81.4 (2.0)	7.4 (1.0)	2.3 (0.5)	3.4 (1.0)	5.5 (1.0)
100Ag-600	76.8 (2.0)	12.5 (1.0)	1.8 (0.5)	3.0 (1.0)	5.9 (1.0)
100Ag-700	73.8 (2.0)	16.1 (1.0)	1.0 (0.5)	3.2 (1.0)	6.0 (1.0)
100Ag-800	77.3 (2.0)	13.9 (1.0)	/	2.9 (0.5)	5.9 (1.0)
100Ag-900	79.4 (2.0)	13.5 (1.0)	/	1.4 (0.5)	5.6 (1.0)
100Ag-1000	85.5 (2.0)	8.7 (1.0)	/	1.1 (0.5)	4.8 (1.0)
100Ag-1100	92.2 (2.0)	4.7 (1.0)	/	0.4 (0.2)	2.8 (0.5)
100Ag-1200	96.8 (2.0)	3.0 (1.0)	/	0.1 (0.2)	/

171

172



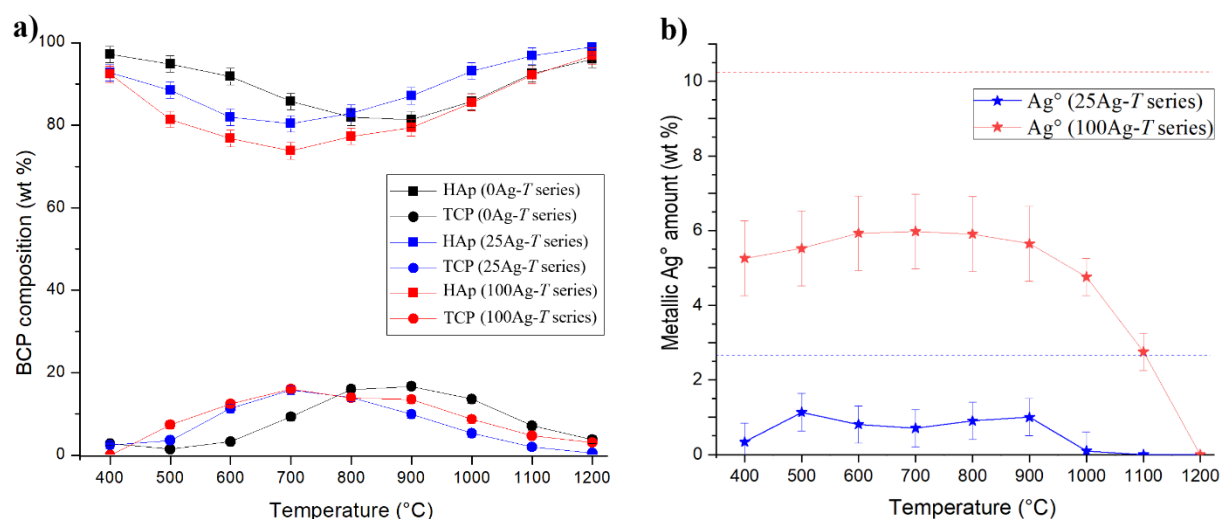
173

174

175

176

**Figure 1.** PXRD patterns from the 25Ag-T series. Scattering signals are mainly those from the HAp phase, and other phases are identified thanks to their intense diffraction peaks (\*: Ag°, #: CaO, x: CaCO<sub>3</sub> and \$: β-TCP).

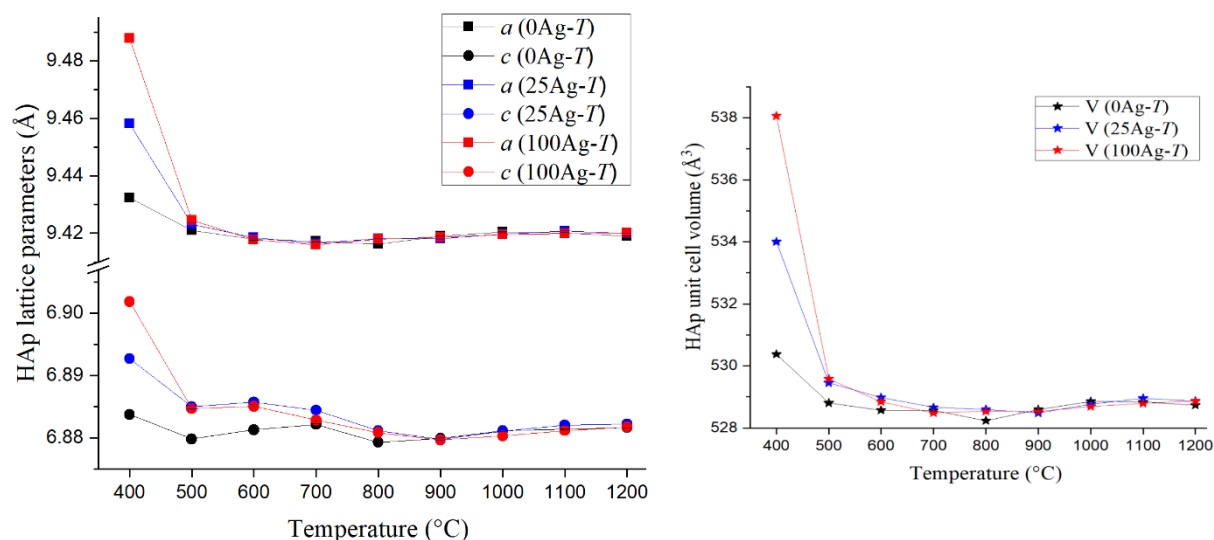


177

178 **Figure 2.** Thermal variation in a) the two main phase contents (squares: HAp; circles: TCP) from the  
 179 BCP samples and b) the metallic silver amount (stars) for the undoped 0Ag-T series (black symbols),  
 180 the 25Ag-T series (blue symbols) and 100Ag-T series (red symbols). Dotted lines indicate the nominal  
 181 silver amounts, and lines are only guides for the eyes.

### 182 3.2. Thermal variation in the HAp structural parameters

183 Thermal variations in the HAp lattice parameters are shown in Figure 3 and collated in Table  
 184 SEI1. Figure 3 clearly shows that the parameters of the HAp network evolved for the lowest  
 185 temperatures and then showed no more variations. The undoped series presents a relatively weak  
 186 contraction between 400 °C and 500 °C for both  $a$  and  $c$  lattice parameters (and consequently for the  
 187 unit cell volume). This contraction is also observed between 400 °C and 500 °C on the basal  $a$  lattice  
 188 parameter for the two silver-doped series, but much more markedly. Concerning the hexagonal  $c$   
 189 lattice parameter, the difference between the undoped and the two doped series extends up to 700  
 190 °C, which of course also affects the unit cell volume difference up to 700 °C. For the lowest  
 191 temperatures, an enlargement of the HAp network is in favour of a calcium-to-silver substitution,  
 192 explained by the larger cationic radius of the  $\text{Ag}^+$  cation: 1.28 Å for  $\text{Ag}^+$  against 1.12 Å for  $\text{Ca}^{2+}$  in  
 193 eightfold coordination [60]. This indication of a silver substitution mechanism to form  $\text{Ag}^+:\text{HAp}$  with  
 194 larger lattice parameters is consistent with previous literature results [32,33,38], but more marked in  
 195 our study. Indeed, the large values found here ( $a = 9.488$  Å and  $c = 6.901$  Å for the 100Ag-400 sample)  
 196 have never been evinced before. Despite the electronic contrast between  $\text{Ag}^+$  and  $\text{Ca}^{2+}$  cations, the last  
 197 Rietveld refinement cycles failed to clearly locate the silver atoms in the hydroxyapatite structure.  
 198 Nevertheless, the indications obtained support the notion of a substitution mechanism at the Ca1 and  
 199 Ca2 sites: the results indicate substitution rates which are too weak, but which are present (silver  
 200 occupancies about 3 % and 5 % – instead of the expected 10 % – for the Ca1 and Ca2 sites respectively),  
 201 and show the absence of chemical elements at the interstitial site within the hexagonal channel (i.e.  
 202 the 2b Wyckoff site). This leads us to privilege the  $\text{Ca}_{10-x}\text{Ag}_x(\text{PO}_4)_6(\text{OH})_{2-x}$  stoichiometry for the doped  
 203  $\text{Ag}^+:\text{HAp}$  phase, and not that proposed by Geng et al.,  $\text{Ca}_{10-x}\text{Ag}_{2x}(\text{PO}_4)_6(\text{OH})_2$  [32], which implies a  
 204 double mechanism by substitution and insertion. Our work on the structural parameters of  
 205 hydroxyapatite enables us to conclude that the HAp silver-doped phase is present in our samples  
 206 from 400 °C to 600 °C. This is correlated with the refined isotropic thermal parameters (see  $B_{\text{iso}}$  in  
 207 Table SEI1) of hydroxyl anions, which are exaggerated in these samples: 25Ag-400, 25Ag-500, 25Ag-  
 208 600, 100Ag-400, 100Ag-500 and 100Ag-600. We will consider below for these temperatures that the  
 209  $\text{Ag}^+:\text{HAp}$  phase presents the nominal stoichiometry, that is to say  $\text{Ca}_{9.75}\text{Ag}_{0.25}(\text{PO}_4)_6(\text{OH})_{1.75}$  for the  
 210 25Ag-T series and  $\text{Ca}_9\text{Ag}_1(\text{PO}_4)_6(\text{OH})$  for the 100Ag-T series, although there is no definitive  
 211 experimental proof for these compositions.



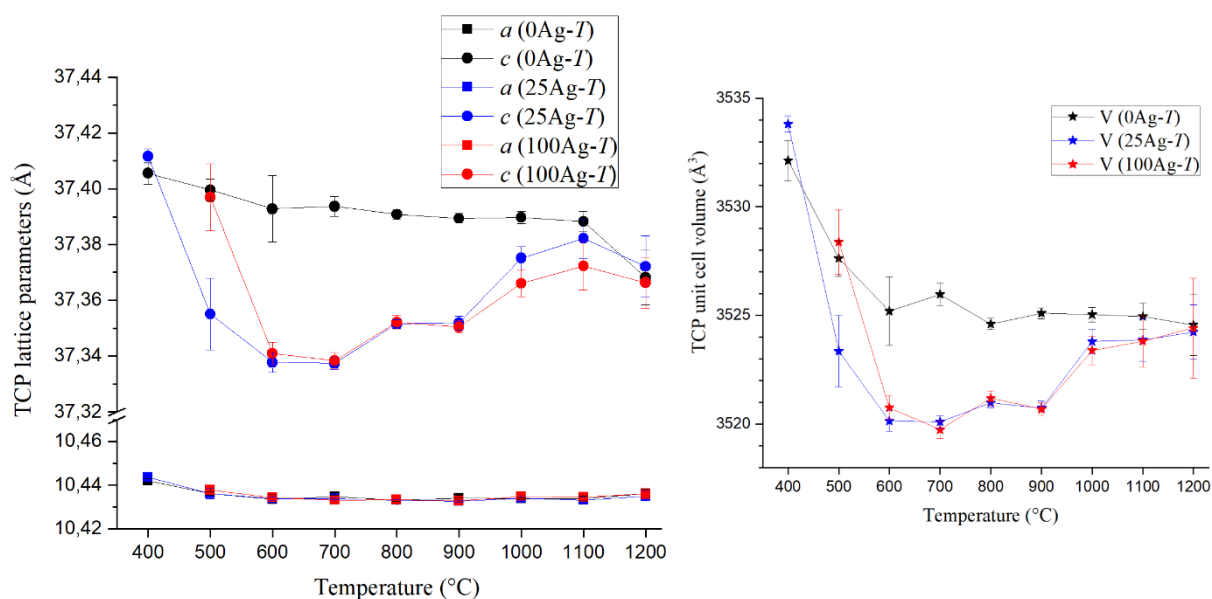
212

213 **Figure 3.** Thermal variation in the HAp lattice parameters for the three series of samples. Left: *a*  
 214 (squares) and *c* (circles) hexagonal lattice parameters, right: unit cell volume (stars). Lines are guides  
 215 for the eyes only.

### 216 3.3. Thermal variation in the $\beta$ -TCP structural parameters

217 Thermal variations in the TCP lattice parameters, shown in Figure 4 and collated in Table SEI2,  
 218 are very different from those presented above for HAp. The basal *a* lattice parameter remained  
 219 constant whatever the synthesis series and heat treatment temperature. On the other hand, variations  
 220 in the axial *c* lattice parameter provide interesting information. The *c* lattice parameter – and  
 221 consequently the unit cell volume – for the two silver-doped series is below the value refined for the  
 222 undoped series, except for the temperature of TCP appearance (400 °C for the 25Ag-*T* series and 500  
 223 °C for the 100Ag-*T* series) and for the higher temperatures (1100 °C and 1200 °C). It corresponds to  
 224 the formation of the ordered calcium-to-silver substitution in  $\beta$ -TCP that leads to the  $\text{AgCa}_{10}(\text{PO}_4)_7$   
 225 compound. This compound is isotypic to  $\beta$ -TCP (trigonal  $R3c$  space group, 18 independent atomic  
 226 positions) with its half-occupied Ca4 site (at the special  $6a$  Wyckoff site [56]) fully filled by  $\text{Ag}^+$  cations  
 227 [55]. The content of the unit cell is then  $\text{Ag}_6\text{Ca}_{60}(\text{PO}_4)_{42}$ ; i.e.  $\text{AgCa}_{10}(\text{PO}_4)_7$  corresponding to  $\text{Ca}_{3-x}\text{Ag}_x(\text{PO}_4)_2$   
 228 with  $x = 0.143$ . This ordered substitution mechanism, leading to a definite compound, is  
 229 accompanied by a decrease in the axial *c* lattice parameter despite the larger size of  $\text{Ag}^+$ : 37.403 Å for  
 230  $\beta$ -TCP [56] against 37.338 Å for  $\text{AgCa}_{10}(\text{PO}_4)_7$  [55]. Thus, the value of the *c* axial lattice parameter  
 231 allows us to determine whether the present TCP phase corresponds to the undoped  $\beta$ -TCP phase or  
 232 the silver-containing  $\text{AgCa}_{10}(\text{PO}_4)_7$  phase. Table SEI2 indicates the TCP phase attribution for each  
 233 sample; either  $\beta$ -TCP (implied undoped  $\text{Ca}_3(\text{PO}_4)_2$ ) or  $\text{AgCa}_{10}(\text{PO}_4)_7$  (called  $\text{Ag}^+$ :TCP here).





234  
 235 **Figure 4.** Thermal variation in TCP lattice parameters for the three series of samples. Left: *a* (squares)  
 236 and *c* (circles) trigonal lattice parameters; right: unit cell volume (stars). Lines are guides for the eyes  
 237 only.

### 238 3.4. Ag location studied by SEM analyses

239 SEM analyses were used to evaluate the silver amount and location in selected samples from the  
 240 doped series. Results from elemental quantifications made with EDS spectroscopy are summarized  
 241 in Table 2. The calculated Ca/P ratio indicates that results should be considered as semi-quantitative  
 242 only because of large deviations from the expected values as well as large variations within a single  
 243 series. This must be connected to the unpolished surface state of the pellets and the use of internal  
 244 calibration lines in the software. However, interesting additional information is provided by these  
 245 analyses.

246 **Table 2.** Quantitative elemental analyses performed by EDS/SEM.

Sample	Analysis	Atomic composition (%)			Calculated ratio		Expected ratio	
		Ca	Ag	P	Ag/Ca	Ca/P	Ag/Ca	Ca/P
0Ag-400	global	65.63	0.00	34.37	0.00	1.91	0.00	1.67
0Ag-700	global	59.80	0.00	40.20	0.00	1.49		
0Ag-1200	global	68.02	0.00	31.98	0.00	2.13		
25Ag-400	global	66.47	2.17	31.37	0.03	2.12	0.03	1.62
25Ag-700	global	60.14	1.43	38.43	0.02	1.56		
25Ag-1200	global	65.48	0.00	34.52	0.00	1.90		
100Ag-400	global	62.39	3.94	33.68	0.06	1.85	0.11	1.50
100Ag-700	global	62.35	3.03	34.61	0.05	1.80		

100Ag-1200	global	60.59	0.00	39.41	0.00	1.54		
25Ag-400 (*)	local_1	65.21	1.24	33.55	0.019	1.94	0.03	1.62
	local_2	40.26	24.64	35.11	n.c. (**)	n.c.		
	local_3	7.40	89.95	2.65	n.c.	n.c.		
	local_4	64.25	1.39	34.36	0.022	1.87		
25Ag-700 (*)	local_5	63.88	0.00	36.12	0.00	1.77		

247 (\*) corresponding images are shown in Figure 6.

248 (\*\*) non-calculated ratio because the analysed area did not correspond to a calcium phosphate.

249

250

251

252

253

254

255

256

257

258

259

260

261

262

263

264

265

266

267

268

269

270

271

272

273

First, results from Table 2 confirm the complete disappearance of silver in doped series after heat treatment at 1200°C. We can conclude that above the melting point of silver, not only did the metallic Ag<sup>0</sup> particles leave the sample, but the calcium phosphate phases were also completely free of Ag<sup>+</sup> cations. The chemical contrast imaging performed with the backscattered electron detector makes it possible to highlight the notion of Ag<sup>0</sup> particles (Figure 5). The use of low magnifications shows the presence of large, micrometric, particles (already present in the 25Ag-400 sample, and in large quantities in the 100Ag-700 sample). Then, thanks to higher magnifications, it is possible to visualize nanometric particles of small size. Figure 5a3 evidences the presence of silver particles of less than 100 nm diameter in 25Ag-400. These particles merged on heating to reach diameters of 200-400 nm in the 25Ag-700 sample (Figure 5b3) and 500-1000 nm in the 100Ag-700 sample (Figure 5c3). Images from Figure 5 clarify the composite feature of the samples.

Finally, local elemental analyses were performed to conclude the SEM characterization (see selected zones in Figure 6). Results from selected areas (EDS shown in Figure 7) are presented in Table 2 for the 25Ag-*T* series. These results confirm that nanoparticles were exclusively composed of silver: metallic Ag<sup>0</sup> as shown in area 3 (and also area 2) in the 25Ag-400 sample. Indeed, the results from the local zone '3' are in favor of particle containing only the silver element (the minor Ca and P contents come from the not really punctual electron beam), and therefore of a metallic nature (i.e. Ag<sup>0</sup> particles). These results also confirm the presence of silver in the phosphate calcium phases for the lowest heat treatment temperatures. Areas 1 and 4 indicate the presence of small amounts of silver, in combination with large amounts of calcium and phosphor at 400°C, corresponding to an Ag<sup>+</sup>:doped HAp phase. This is no longer true at 700 °C, where the calcium and phosphorus elements are completely separated from the silver element: area 5 in sample 25Ag-700 is only composed of Ca and P corresponding to undoped calcium phosphate compound (Figure 7 and Table 2).

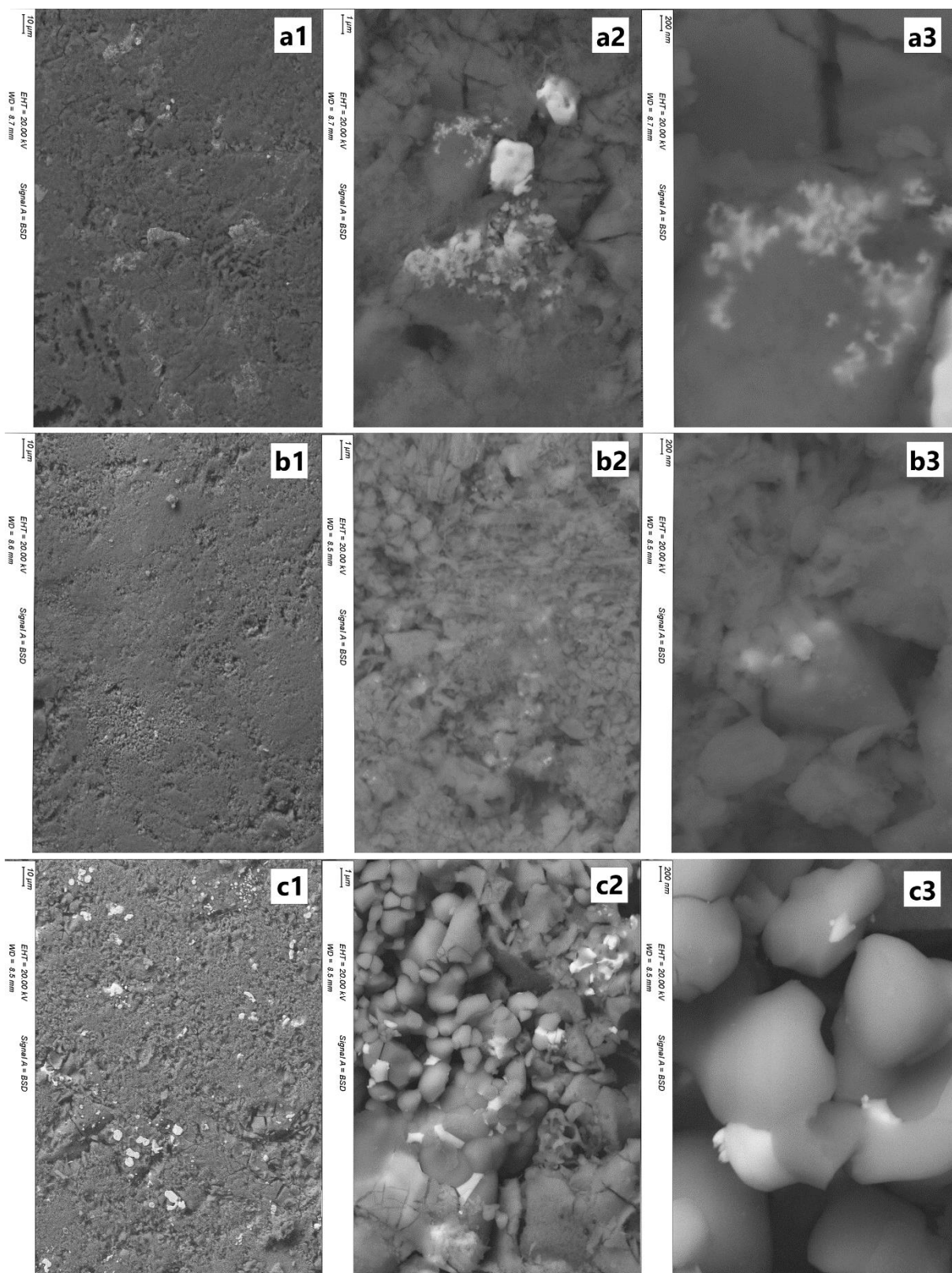
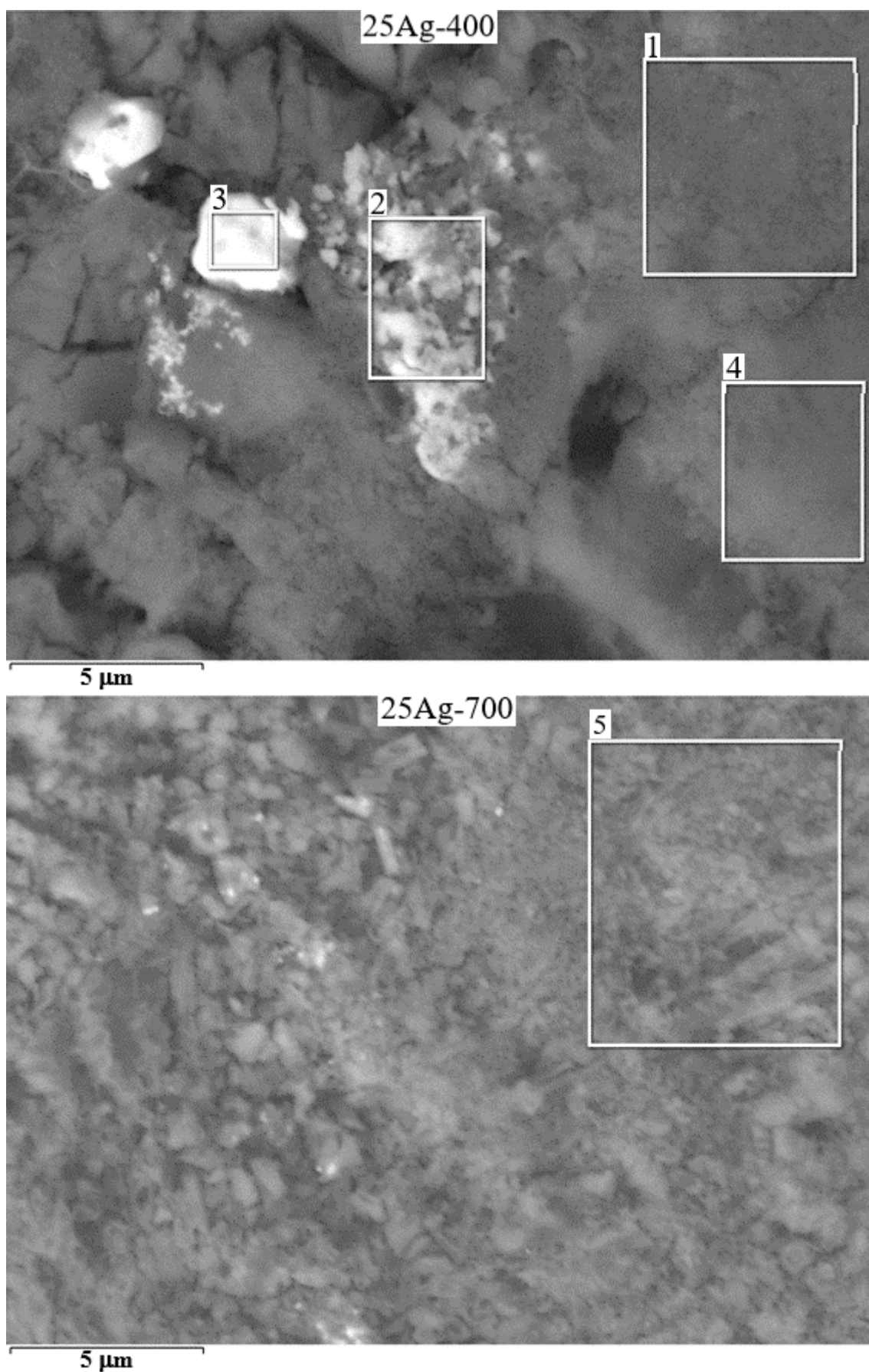


**Figure 5.** Electron Backscattered SEM images showing the metallic silver particles in the samples. a) 25Ag-400; b) 25Ag-700 and c) 100Ag-700 samples using 1: x500, 2: x5k and 3: x20k magnifications.

274  
275  
276

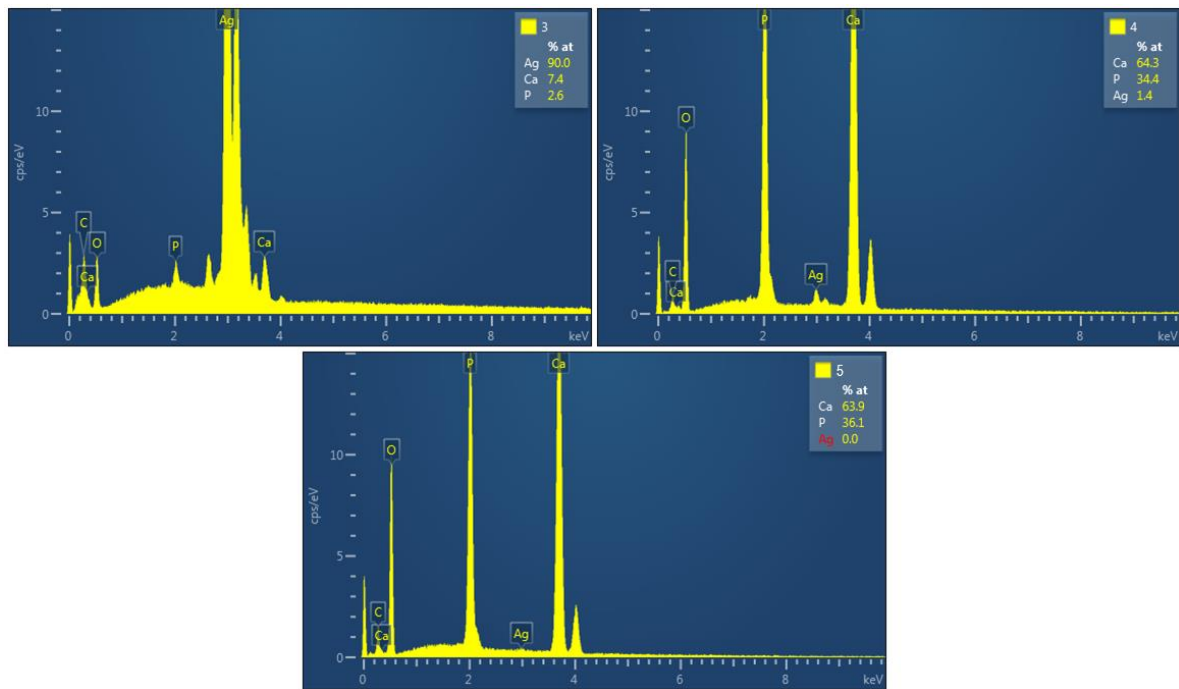


277  
278  
279

**Figure 6.** Electron Backscattered SEM photographs used for local elemental analyses (presented in Table 2) of the 25Ag-400 and 25Ag-700 samples.



280



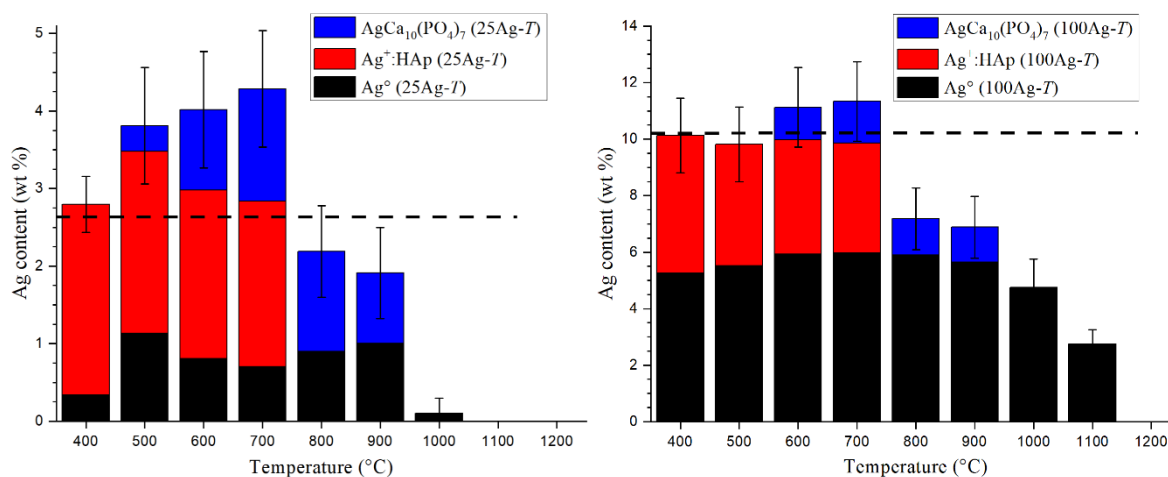
281

282 **Figure 7.** Selected local EDS analyses (presented in Table 2) from zones '3' and '4' of the 25Ag-400  
 283 sample and from zone '5' of the 25Ag-700 sample (shown in Figure 6).

284

#### 285 4-. Discussion

286 The results presented above evidence three distinct locations for silver atoms in the synthesized  
 287 BCP samples, including two distinct chemical states (metallic and ionic). A part of the introduced  
 288 silver cations is found in the metallic state, in the form of nanoparticles, already present at 400 °C.  
 289 The remainder is in the cationic form in substitution for calcium cations, either in the HAp phase (at  
 290 low temperatures: from 400 °C to 600 °C) or in the TCP phase (at the following temperatures and up  
 291 to 1000 °C). From 1000 °C silver leaves the samples, especially because of the melting point of Ag<sup>0</sup>  
 292 (962 °C). The cumulative amounts of located silver atoms are shown in Figure 8 for both the 25Ag-*T*  
 293 and 100Ag-*T* doped series. It appears that calculations for the lowest (400 °C) temperature are in good  
 294 agreement with the nominal introduced amounts (i.e. 2.67 wt % for the 25Ag-*T* series and 10.22 wt %  
 295 for the 100Ag-*T* series). We then observe an overestimation of the silver content up to 600°C, before  
 296 seeing it start to plummet at 700 °C. These fluctuations around the expected values indicate that the  
 297 amount of silver in the HAp phase is overestimated above 500 °C, and conversely the amount of  
 298 silver in substitution in β-TCP is certainly underestimated from 800 °C upwards.



299

300

301

302

303

**Figure 8.** Cumulative silver amount taken from metallic Ag° (black), substituted HAp (red) and AgCa<sub>10</sub>(PO<sub>4</sub>)<sub>7</sub> (or substituted TCP, blue) for the 25Ag-T series (left) and the 100Ag-T series (right). Dotted lines indicate the nominal silver amounts, and error bars correspond to cumulative standard deviation considering the three phases.

304

305

306

307

308

309

310

311

312

313

314

315

316

317

318

319

Nanoparticles of metallic silver therefore formed very quickly in our samples by the autogenous reduction of silver nitrate. The set of samples can thus be considered as a Ag°/BCP composite. However, at low temperatures, we also observe the formation of a silver-doped Ag<sup>+</sup>:HAp phase whose composition is close to the nominal composition (i.e. Ca<sub>9.75</sub>Ag<sub>0.25</sub>(PO<sub>4</sub>)<sub>6</sub>(OH)<sub>1.75</sub> for the 25Ag-T series and Ca<sub>9</sub>Ag<sub>1</sub>(PO<sub>4</sub>)<sub>6</sub>(OH) for the 100Ag-T series). Beyond 400 °C, this doped Ag<sup>+</sup>:HAp phase persists while gradually lowering its doping element content. The drop in the doping rate was notably predictable by observing the variations in the HAp lattice parameters between 400 °C and 700 °C (Figure 3). Both *a* and *c* lattice parameters of the Ag<sup>+</sup>:HAp phase are vastly superior to those from the undoped series at 400 °C. This difference fades at 500 °C and disappears at 700 °C. SEM analyses confirmed the presence of dopant in the calcium phosphate phase at 400 °C, followed by its exclusion at 700 °C. Concomitantly, cationic Ag<sup>+</sup> substitutes calcium cations into the β-TCP phase, which stabilizes around 700 °C. First, the AgCa<sub>10</sub>(PO<sub>4</sub>)<sub>7</sub> definite compound is formed; it is distinguishable from the undoped β-TCP phase thanks to the smaller *c* lattice parameter (Figure 4). The underestimation of silver content from 800 °C upwards suggests that the Ag<sup>+</sup> amount in the TCP phase continues to increase; however, no experimental proof has been brought to support this.

320

321

322

323

324

325

326

327

328

329

330

331

The characterization of the doped Ag<sup>+</sup>:HAp phase with increased lattice parameters, by comparison with an undoped HAp lattice, has already been reported in the literature. This is notably the case in the study of Geng et al. [32], where the Ca<sub>10-x</sub>Ag<sub>2x</sub>(PO<sub>4</sub>)<sub>6</sub>(OH)<sub>2</sub> doped composition was considered. This nominal composition suggests two kinds of doping mechanism: only half of the silver cations (*x* value) can substitute calcium cations into the Ca1 or Ca2 crystallographic sites of the HAp crystal structure. The second half of silver cations (to reach the 2*x* doping level) must be located at interstitial sites. Our crystallographic study, based on Rietveld refinement, did not enable us to highlight the presence of silver cations at interstitial crystallographic sites, not to mention that this situation is not preponderant for large cations like Ag<sup>+</sup>. For these reasons we preferred to note the chemical composition of the doped Ag<sup>+</sup>:HAp phase as follows: Ca<sub>10-x</sub>Ag<sub>x</sub>(PO<sub>4</sub>)<sub>6</sub>(OH)<sub>2-x</sub>, in which only the substitution mechanism was considered in agreement with the paper by Badroun et al. [61]. However, we must admit that our Rietveld refinements did not make it possible to clearly quantify the silver substitution rates at both the Ca1 and Ca2 crystallographic sites in the HAp structure.

332

## 5-. Conclusion

333

334

335

336

During the past decade, several studies have been devoted to silver incorporation in HAp (or BCP) samples due to their high potential for biomaterial applications, namely because of the well-known bactericide properties of silver. Unanimously, the results have shown a very interesting bactericidal effect following the doping of calcium phosphates with silver. However, the material

337 aspect of the samples studied in the literature showed some disparities, in particular due to a lack of  
338 understanding of the doping mechanism. Some works mention metallic silver nanoparticles; others  
339 focus on cationic substitution in phosphate phases. The results presented in the present paper are  
340 especially devoted to the description of the mechanism by which silver is incorporated into BCP  
341 samples. This work follows the experience previously acquired on the BCP doping mechanism of the  
342 first-row transition elements. It appears that both electronic states are simultaneously present in the  
343 silver-doped samples: metallic  $\text{Ag}^0$  and cationic  $\text{Ag}^+$ . Synthesized samples are composites comprising  
344 closely-mixed  $\text{Ag}^0$  nanoparticles and  $\text{Ag}^+$ -doped calcium phosphate phases. At the lowest  
345 temperature (400 °C), it is the HAp phase which presents a silver-to-calcium substitution leading to  
346 the doped  $\text{Ca}_{10-x}\text{Ag}_x(\text{PO}_4)_6(\text{OH})_{2-x}$  compounds. Then, by increasing the temperature (above 600 °C) the  
347  $\text{Ag}^+$  cations migrate to the  $\beta$ -TCP phase to form the definite  $\text{Ca}_{10}\text{Ag}(\text{PO}_4)_7$  compound corresponding  
348 to  $\text{Ca}_{3-x}\text{Ag}_{2x}(\text{PO}_4)_2$  with  $x = 0.143$  (i.e.  $\text{Ca}_{2.857}\text{Ag}_{0.286}(\text{PO}_4)_2$ ). Finally, the composite aspect of the prepared  
349 samples disappears above 1000 °C because the relatively low melting point of silver (962 °C). In the  
350 light of these results, it appears important for the study of biological properties to distinguish the  
351 behaviour in biological conditions of metallic silver nanoparticles from that of substituted cationic  
352  $\text{Ag}^+$ , particularly in terms of bactericidal power and release rate/kinetics in the human body.

353 **Acknowledgments:** The authors warmly thank Anne-Marie Gelineau for the electron microscopy performed at  
354 2MATech - Clermont-Ferrand, a few days before her retirement. Reviewers and guest editor, Francesco Capitelli,  
355 are also grateful for their questions and comments that have improved the content and understanding if this  
356 paper.

## 357 References

- 358 [1] Dorozhkin, S.V. Biocomposites and hybrid biomaterials based on calcium orthophosphates.  
359 *Biomaterials*. **2011**, *1*, 3–56.
- 360 [2] Dahl, S.G.; Allain, P.; Marie, P.J.; Mauras, Y.; Boivin, G.; Ammann, P.; Tsouderos, Y.; Delmas, P.D.;  
361 Christiansen, C. Incorporation and distribution of strontium in bone. *Bone* **2001**, *8*, 446–453.
- 362 [3] Lagier, R.; Baud, C.A. Magnesium whitlockite, a calcium phosphate crystal of special interest in  
363 pathology. *Pathol. Res. Pract.* **2003**, *199*, 329–335.
- 364 [4] Lee, R.S.; Kayser, M.V.; Ali, S.Y. Calcium phosphate microcrystal deposition in the human  
365 intervertebral disc. *J. Anat.* **2006**, *208*, 13–19.
- 366 [5] Rey, C.; Combes, C.; Drouet, C.; Glimcher, M.J. Bone mineral: update on chemical composition and  
367 structure. *Osteoporos Int.* **2009**, *20*, 1013–1021.
- 368 [6] Cazalbou, S.; Combes, C.; Eichert, D.; Rey, C. Adaptive physico-chemistry of bio-related calcium  
369 phosphates. *J. Mater. Chem.* **2004**, *14*, 2148–2153.
- 370 [7] Elliot, J.C. Structure and chemistry of the apatite and other calcium orthophosphates, Amsterdam:  
371 Elsevier, **1994**.
- 372 [8] Turkoz, M.; Atilla, A.O.; Evis, Z. Silver and fluoride doped hydroxyapatite: Investigation by  
373 microstructure, mechanical and antibacterial properties, *Ceram. Int.* **2013**, *39* 8925–8931.
- 374 [9] Diaz, M.; Zia, R.; Sameemi, F.; Ikram, H.; Bashir, F. In vitro antimicrobial activity of ZnO based  
375 glass-ceramics against pathogenic bacteria. *J. Mater. Sci. Mater. Med.* **2015**, *26*:268.
- 376 [10] Khan, M.S.; ur Rehman, S.; Ali, M.A.; Sultan, B.; Sultan, S. Infection in orthopedic implant  
377 surgery, its risk factors and outcome. *J. Ayub Med. Coll. Abbottabad* **2008**, *20*, 23–25.
- 378 [11] Cremet, L.; Corvec, S.; Bemer, P.; Bret, L.; Lebrun, C.; Lesimple, B.; Miegerville, A.F.; Reynaud, A.;  
379 Lepelletier, D.; Caroff, N. Orthopaedic-implant infection by Escherichia coli: molecular and  
380 phenotypic analysis of the causative strains. *J. Infect.* **2012**, *64*, 169–175.
- 381 [12] Salwiczek, M.; Qu, Y.; Gardiner, J.; Strugnell, R.A.; Lithgow, T.; McLean, K.M.; Thissen, H.  
382 Emerging rules for effective antimicrobial coatings. *Trends Biotechnol.* **2014**, *32*, 82–90.
- 383 [13] Nasser, S. Prevention and treatment of sepsis in total hip replacement surgery. *Orthop. Clin. North*  
384 *Am.* **1992**, *23*, 265–277.
- 385 [14] Li, P.L.; Zamora, J.; Bentley, G. The results at ten years of the Insall-Burstein II total knee  
386 replacement: clinical, radiological and survivorship studies. *J. Bone Joint Surg. Br.* **1999**, *81*, 647–653.

- 387 [15] Hendriks, J.G.E.; van Horn, J.R.; van der Mei, H.C.; Busscher, H.J. Background of antibiotic-  
388 loaded bone cement and prosthesis-related infection. *Biomaterials* **2004**, *25*, 545-556.
- 389 [16] Fan, J.C.H.; Hung, H.H.; Fung, K.Y. Infection in primary total knee replacement. *Hong Kong Med.*  
390 *J.* **2008**, *14*, 40-45.
- 391 [17] Sygnatowicz, M.; Keyshar, K.; Tiwari, A. Antimicrobial properties of silver-doped  
392 hydroxyapatite nano-powders and thin films. *Bio. Biomed. Mater.* **2010**, *62*, 65-70.
- 393 [18] Rauschmann, M.A.; Wichelhaus, T.A.; Stirnal, V.; Dingeldein, E.; Zichner, L.; Schnettler, R.; Alt,  
394 V. Nanocrystalline hydroxyapatite and calcium sulphate as biodegradable composite carrier material  
395 for local delivery of antibiotic in bone infections. *Biomaterials* **2005**, *26*, 2677-2684.
- 396 [19] Baradari, H.; Damia, C.; Dutreih-Colas, M.; Laborde, E.; Pecout, N.; Champion, E.; Chulia, D.;  
397 Viana, M. Calcium phosphate porous pellets as drug delivery systems: effect of drug carrier  
398 composition on drug loading and in vitro release. *J. Eur. Ceram. Soc.* **2012**, *32*, 2679-2690.
- 399 [20] Clement, J.L.; Jarrett, P.S. Antibacterial silver. *Metal-Based Drugs* **1994**, *1*, 467-482.
- 400 [21] Marambio-Jones, C.; Hoek, E.M.V. A review of the antibacterial effects of silver nanomaterials  
401 and potential implications for human health and the environment. *J. Nano. Res.* **2010**, *12*, 1531-1551.
- 402 [22] Iqbal, N.; Kadir, A.R.M.; Malek, N.N.A.N.; Mahmood, H.N.; Murali, R.M.; Kamarul, T. Rapid  
403 microwave assisted synthesis and characterization of nanosized silver-doped hydroxyapatite with  
404 antibacterial properties. *Mater. Lett.* **2012**, *89*, 118-122.
- 405 [23] Ning, C.; Wang, X.; Li, L.; Zhu, Y.; Li, M.; Yu, P.; Zhou, L.; Zhou, Z.; Chen, J.; Tan, G.; Zhang, Y.;  
406 Wang, Y.; Mao, C. Concentration ranges of antibacterial cations for showing the highest antibacterial  
407 efficacy but the least cytotoxicity against mammalian cells: implications for a new antibacterial  
408 mechanism. *Chem. Res. Toxicol.* **2015**, *28*, 1815-1822.
- 409 [24] Kim, T.N.; Feng, Q.L.; Kim, J.O.; Wu, J.; Wang, H.; Chen, G.C.; Cui, F.Z. Antimicrobial effects of  
410 metal ions (Ag<sup>+</sup>, Cu<sup>2+</sup>, Zn<sup>2+</sup>) in hydroxyapatite. *J. Mater. Sci. Mater. Med.* **1998**, *8*, 129-134.
- 411 [25] Feng, Q.L.; Wu, J.; Chen, G.Q.; Cui, F.Z.; Kim, T.N. A mechanistic study of the antibacterial effect  
412 of silver ions on Escherichia coli and staphylococcus aureus. *J. Biomed. Mater. Res.* **2000**, *52*, 662-668.
- 413 [26] Rameshbabu, N.; Sampath Kumar, T.S.; Prabhakar, T.G.; Sastry, V.S.; Murty, K.V.G.K.; Prasad  
414 Rao, K. Antibacterial nanosized silver substituted hydroxyapatite: synthesis and characterization. *J.*  
415 *Biomed. Mater. Res. A* **2007**, *80*, 581-591.
- 416 [27] Klaseen, H.J. Historical review of the use of silver in the treatment of burns: I. Early uses. *Burns*  
417 **2000**, *26*, 117-130.
- 418 [28] Gosheger, G.; Harges, J.; Ahrens, H.; Streitburger, A.; Buerger, H.; Erren, M.; Gonsel, A.; Kemper,  
419 F.H.; Winkelmann, W.; von Eiff, C. Silver-coated megaendoprostheses in a rabbit model – an analysis  
420 of the infection rate and toxicological side effects. *Biomaterials* **2004**, *25*, 5547-5556.
- 421 [29] Ciobanu, C.S.; Iconaru, S.L.; Pasuk, I.; Vasile, B.S.; Lupu, A.R.; Hermenean, A.; Dinischiotu, A.;  
422 Predoi, D. Structural properties of silver doped hydroxyapatite and their biocompatibility. *Mater. Sci.*  
423 *Eng. C* **2013**, *33*, 1395-1402.
- 424 [30] Jadalannagari, S.; Deshmukh, K.; Ramanan, S.R.; Kowshik, M. Antimicrobial activity of  
425 hemocompatible silver doped hydroxyapatite nanoparticles synthesized by modified sol-gel  
426 technique. *Appl. Nanosci.* **2014**, *4*, 133-141.
- 427 [31] Fu, C.; Zhang, X.; Savino, K.; Gabrys, P.; Gao, Y.; Chaimayo, W.; Miller, B.L.; Yates, M.Z.  
428 Antimicrobial silver-hydroxyapatite composite coating through two-stage electrochemical synthesis.  
429 *Surf. Coat. Tech.* **2016**, *301*, 13-19.
- 430 [32] Geng, Z.; Cui, Z.; Li, Z.; Zhu, S.; Liang, Y.; Liu, Y.; He, X.; Yu, X.; Wang, R.; Yang, W. Strontium  
431 incorporation to optimize the antibacterial and biological characteristics of silver-substituted  
432 hydroxyapatite coating. *Mater. Sci. Eng. C* **2016**, *58*, 467-477.
- 433 [33] Gokcekaya, O.; Webster, T.J.; Ueda, K.; Narushima, T.; Ergun, C. In vitro performance of Ag-  
434 incorporated hydroxyapatite and its adhesive porous coating deposited by electrostatic spaying.  
435 *Mater. Sci. Eng. C* **2017**, *77*, 556-564.
- 436 [34] Wang, J.; Gong, X.; Hai, J.; Li, T. Synthesis of silver-hydroxyapatite composite with improved  
437 antibacterial properties. *Vacuum* **2018**, *152*, 132-137.



- 438 [35] Riaz, M.; Zia, R.; Ijaz, A.; Hussain, T.; Mohsin, M.; Malik, A. Synthesis of monophasic Ag doped  
439 hydroxyapatite and evaluation of antibacterial activity. *Mater. Sci. Eng. C* **2018**, *90*, 308-313.
- 440 [36] Dubnika, A.; Loca, D.; Rudovica, V.; Parekh, M.B.; Berzina-Cimdina, L. Functionalized silver-  
441 doped hydroxyapatite scaffolds for controlled simultaneous silver ion and drug delivery. *Ceram. Int.*  
442 **2017**, *43*, 3698-3705.
- 443 [37] Zhang, X.; Chaimayo, W.; Yang, C.; Yao, J.; Miller, B.L.; Yates, M.Z. Silver-hydroxyapatite  
444 composite coatings with enhances antimicrobial activities through heat treatment. *Surf. Coat. Tech.*  
445 **2017**, *325*, 39-45.
- 446 [38] Gokcekaya, O.; Ueda, K.; Narushima, T.; Ergun, C. Synthesis and characterization of Ag-  
447 containing calcium phosphates with various Ca/P ratios. *Mater. Sci. Eng. C* **2015**, *53*, 111-119.
- 448 [39] Iqbal, N.; Kadir, M.R.A.; Mahmood, N.H.; Salim, N.; Froemming, G.R.A.; Balaji, H.R.; Kamarul,  
449 T. Characterization, antibacterial and in-vitro compatibility of zinc-silver doped hydroxyapatite  
450 nanoparticles prepared through microwave synthesis. *Ceram. Int.* **2014**, *40*, 4507-4513.
- 451 [40] Kaygili, O.; Keser, S.; Dorozhkin, S.V.; Yakuphanoglu, F.; al-Ghamdi, A.A.; Kirbag, S.; Sertkaya,  
452 D.; Ates, T.; Gursoy, N.C. Structural and dielectrical properties of Ag- and Ba-substituted  
453 hydroxyapatites. *J. Inorg. Organomet. Polym.* **2014**, *24*, 1001-1008.
- 454 [41] Liu, X.; Mou, Y.; Wu, S.; Man, H.C. Synthesis of silver-incorporated hydroxyapatite  
455 nanocomposites for antimicrobial implant coatings. *Appl. Surf. Sci.* **2013**, *273*, 748-757.
- 456 [42] Vukomanovic, M.; Bracko, I.; Poljansek, I.; Uskokovic, D.; Skapin, S.D.; Suvorov, D. The growth  
457 of silver nanoparticles and their combination with hydroxyapatite to form composites via a  
458 sonochemical approach. *Cryst. Growth Des.* **2011**, *11*, 3802-3812.
- 459 [43] Chen, Y.; Zheng, X.; Xie, Y.; Ji, H.; Ding, C.; Li, H.; Dai, K. Silver release from silver-containing  
460 hydroxyapatite coatings. *Surf. Coat. Tech.* **2010**, *205*, 1892-1896.
- 461 [44] Chen, W.; Oh, S.; Ong, A.P.; Oh, N.; Liu, Y.; Courtney, H.S.; Appleford, M.; Ong, J.L. Antibacterial  
462 and osteogenic properties of silver-containing hydroxyapatite coatings produced using sol-gel  
463 process. *J. Biomed. Mater. Res. A* **2007**, *82*, 899-906.
- 464 [45] Chen, W.; Liu, Y.; Courtney, H.S.; Bettenga, M.; Agrawal, C.M.; Bumgardner, J.D.; Ong, J.L. In  
465 vitro anti-bacterial and biological properties of magnetron co-sputtered silver-containing  
466 hydroxyapatite coating. *Biomaterials* **2006**, *27*, 5512-5517.
- 467 [46] Feng, Q.L.; Kim, T.N.; Wu, J.; Park, E.S.; Kim, J.O.; Lim, D.Y.; Cui, F.Z. Antibacterial effects of  
468 Ag-HAp thin films on alumina substrates. *Thin Sol. Films* **1998**, *335*, 214-219.
- 469 [47] Shirkhazadeh, M.; Azadegan, M.; Liu, G.Q. Bioactive delivery systems for the slow release of  
470 antibiotics: incorporation of Ag<sup>+</sup> ions into micro-porous hydroxyapatite coatings. *Mater. Lett.* **1995**,  
471 *24*, 7-12.
- 472 [48] Renaudin, G.; Gomes, S.; Nedelec, J.-M. First-row transition metal doping in calcium phosphate  
473 bioceramics: a detailed crystallographic study. *Materials* **2017**, *10*, 92-113.
- 474 [49] Gomes, S.; Nedelec, J.-M.; Renaudin, G. On the effect of temperature on the insertion of zinc into  
475 hydroxyapatite. *Acta Biomater.* **2012**, *8*, 1180-1189.
- 476 [50] Gomes, S.; Kaur, A.; Nedelec, J.-M.; Renaudin, G. X-ray Absorption Spectroscopy shining  
477 (synchrotron) light onto the insertion of Zn<sup>2+</sup> in calcium phosphate ceramics and its influence on their  
478 behaviour in biological conditions. *J. Mater. Chem. B* **2014**, *2*, 536-545.
- 479 [51] Gomes, S.; Nedelec, J.-M.; Jallot, E.; Sheptyakov D.; Renaudin, G. Unexpected mechanism of Zn<sup>2+</sup>  
480 insertion in calcium phosphate bioceramics. *Chem. Mat.* **2011**, *23*, 3072-3085.
- 481 [52] Gomes, S.; Kaur, A.; Grenèche, J.-M.; Nedelec, J.-M.; Renaudin, G. Atomic scale modeling of iron-  
482 doped biphasic calcium phosphate bioceramics. *Acta Biomater.* **2017**, *50*, 78-88.
- 483 [53] Gomes, S.; Vichery, C.; Descamps, S.; Martinez, H.; Kaur, A.; Jacobs, A.; Nedelec, J.-M.; Renaudin,  
484 G. Cu-doping of calcium phosphate bioceramics: from mechanism to the control of cytotoxicity. *Acta*  
485 *Biomater.* **2018**, *65*, 462-474.
- 486 [54] Rodriguez-Carvajal, J. PROGRAM *FullProf.2k* – version 3.20; Laboratoire Léon Brillouin (CEA-  
487 CNRS): Saclay, France, 2005; FullProf.2k manual available on [http://www-](http://www-llb.cea.fr/fullweb/fp2k/fp2k_divers.htm)  
488 [llb.cea.fr/fullweb/fp2k/fp2k\\_divers.htm](http://www-llb.cea.fr/fullweb/fp2k/fp2k_divers.htm). See also Rodriguez-Carvajal, J.; Roisnel, T. *EPDIC-8*; May 23-  
489 26, 2002; Trans. Tech. Publication: Uppsala, Sweden; *Mater. Sci. Forum* 2004; 123:443.

- 490 [55] Strutynska, N.Y.; Zatovsky, I.V.; Ogorodnyk, I.V.; Slobodyanik, N.S. Rietveld refinement of  
491  $\text{AgCa}_{10}(\text{PO}_4)_7$  from X-ray powder data. *Acta Cryst. E* **2013**, *69*, i23.
- 492 [56] Yashima, M.; Sakai, A.; Kamiyama, T.; Hoshikawa, A. Crystal structure analysis of beta-  
493 tricalcium phosphate  $\text{Ca}_3(\text{PO}_4)_2$  by neutron powder diffraction. *J. Sol. State Chem.* **2003**, *175*, 272–277.
- 494 [57] Owen, E.A.; Yates, E.L. Precision measurement of crystal parameters. *Phil. Mag.* **1933**, *15*, 472-  
495 488.
- 496 [58] Mocanu, A.; Furtos, G.; Rapuntean, S.; Horovitz, O.; Flore, C.; Garbo, C.; Danisteanu, A.;  
497 Rapuntean, G.; Prejmerean, C.; Tomoaia-Cotisel, M. Synthesis; characterization and antimicrobial  
498 effects of composites based on multi-substituted hydroxyapatite and silver nanoparticles. *Appl. Surf.*  
499 *Sci.* **2014**, *298*, 225-235.
- 500 [59] Singh, B.; Dubey, A.K.; Kumar, S.; Saha, N.; Basu, B.; Gupta, R. In vitro biocompatibility and  
501 antimicrobial activity of wet chemically prepared  $\text{Ca}_{10-x}\text{Ag}_x(\text{PO}_4)_6(\text{OH})_2$  ( $0.0 \leq x \leq 0.5$ ) hydroxyapatites.  
502 *Mater. Sci. Eng. C* **2011**, *31*, 1320-1329.
- 503 [60] Shannon, R.D. Revised effective ionic radii and systematic studies of interatomic distances in  
504 halides and chalcogenides, *Acta Cryst. A* **1976**, *32*, 751-767.
- 505 [61] Badrour, L.; Sadel, A.; Zahir, M.; Kimakh, L.; el Hajbi, A. Synthesis and physical and chemical  
506 characterization of  $\text{Ca}_{10-x}\text{Ag}_x(\text{PO}_4)_6(\text{OH})_{2-x}\square_x$  apatites. *Ann. Chim. Sci. Mat.* **1998**, *23*, 61-64.